doi:10.1038/nature09786

1 Characteristics of the Minimum of Solar Cycle 23

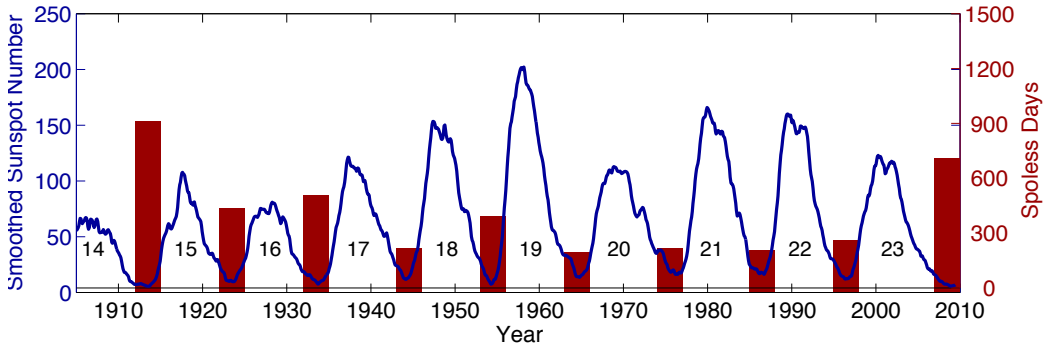

Figure 1: Sunspot cycles over the last century. The blue curve shows the cyclic variation in the number of sunspots (left-hand y-axis) with time (x-axis). The red bars shows the cumulative number of sunspot-less days (right-hand y-axis) between successive maximum; the minimum of sunspot cycle 23 was the longest in the space age with the largest number of spotless days. Nonetheless, the recorded sunspot history shows solar cycles 13 and 14 had even larger number of spotless days; hence, although the recently concluded minimum was unusual, it is not unique..

The solar magnetic cycle goes through periods of successive maxima and minima in activity which is manifested in a variation in the number of sunspots observed on the solar surface. The minimum of solar activity is often parameterized by the number of days without sunspots (i.e. spotless days). The recently concluded solar minimum following sunspot cycle 23 was unusually long, with the largest number of spotless days recorded in the space age (see Figure 1). Moreover, this minimum was also characterized by a relatively weak solar polar field strength as compared to

the previous three cycles, for which direct polar field observations exists.

2 The Dynamo Model

In our simulation we solve the kinematic, axisymmetric dynamo equations:

$$\frac{\partial A}{\partial t} + \frac{1}{s}\left[\mathbf{v}_p \cdot \nabla(sA)\right] = \eta\left(\nabla^2 - \frac{1}{s^2}\right)A, \tag{1}$$

$$\frac{\partial B}{\partial t} + s\left[\mathbf{v}_p \cdot \nabla\left(\frac{B}{s}\right)\right] + (\nabla \cdot \mathbf{v}_p)B = \eta\left(\nabla^2 - \frac{1}{s^2}\right)B + s\left([\nabla \times (A\hat{\mathbf{e}}_\phi)] \cdot \nabla\Omega\right) + \frac{1}{s}\frac{\partial \eta}{\partial r}\frac{\partial (sB)}{\partial r}, \tag{2}$$

where A is the ϕ-component of the potential vector (from which B_r and B_θ can be obtained), B is the toroidal field (B_ϕ), v_p is the meridional flow, Ω the differential rotation, η the turbulent magnetic diffusivity and $s = r\sin(\theta)$. Conspicuous by its absence is the so-called poloidal source (traditionally known as the dynamo α-effect); in this work we introduce a more accurate treatment of the Babcock-Leighton[12,13] poloidal field regeneration algorithm as a discreet process composed of individual bipolar sunspot pairs (also known as Active Regions, ARs; more below). Kinematic dynamo models based on this Babcock-Leighton poloidal field regeneration mechanism have been successful in reproducing the large-scale properties of the solar cycle[6] and is strongly supported by recent observations[29]. We also need to define three more ingredients: meridional flow, differential rotation and turbulent magnetic diffusivity. We use appropriate choices for these physical ingredients which make our simulations relevant for the Sun; these are discussed in the ensuing sections. More details regarding kinematic dynamo models can be found in a review by Charbonneau[6] and

references therein.

3 Modeling Individual Active Regions

It is currently believed that the recreation of poloidal field is caused primarily by the emergence of ARs, and their subsequent diffusion and transport towards the poles; an idea first introduced by Babcock[12] and further elaborated by Leighton[13]. Due to the crucial role of ARs, modeling their emergence accurately within the dynamo process is important. In order to do this, we follow an idea proposed by Durney[25] (and further elucidated by Nandy & Choudhuri[26]) of using ring duplets, although with an improved version which addresses the two main deficiencies of the earlier algorithms: strong sensitivity to changes in grid resolution and the introduction of sharp discontinuities on the ϕ component of the potential vector A.

We define the ϕ component of the potential vector A corresponding to an AR as:

$$A_{ar}(r,\theta) = K_0 A(\Phi) F(r) G(\theta), \tag{3}$$

where $K_0 = 400$ is a constant we introduce to insure super-critical solutions and $A(\Phi)$ defines the strength of the ring-duplet and is determined by flux conservation. $F(r)$ is defined as

$$F(r) = \begin{cases} 0 & r < R_\odot - R_{ar} \\ \frac{1}{r}\sin^2\left[\frac{\pi}{2R_{ar}}(r - (R_\odot - R_{ar}))\right] & r \geq R_\odot - R_{ar} \end{cases}, \tag{4}$$

where $R_\odot = 6.96 \times 10^8$ m corresponds to the radius of the Sun and $R_{ar} = 0.15 R_\odot$ represents the penetration depth of the AR. Finally, $G(\theta)$ is easier to define in integral form and in the context of the geometry of the radial component of the magnetic field on the surface. In Figure 2-a we

present a plot of the two super-imposed polarities of an AR after being projected on the r-θ plane. In order to properly describe such an AR we need to define the following quantities: the co-latitude of emergence θ_{ar}, the diameter of each polarity of the duplet Λ, for which we use a fixed value of 6^o (heliocentric degrees) and the latitudinal distance between the centers $\chi = \arcsin[\sin(\gamma)\sin(\Delta_{ar})]$, which in turn depends on the angular distance between polarity centers $\Delta_{ar} = 6^o$ and the AR tilt angle γ; χ is calculated using the spherical law of sines. In terms of these quantities, the latitudinal dependence for each polarity is determined by the following piecewise function (use the top signs for the positive polarity and the lower for negative):

$$B_{\pm}(\theta) = \begin{cases} 0 & \theta < \theta_{ar} \mp \frac{\chi}{2} - \frac{\Lambda}{2} \\ \pm\frac{1}{\sin(\theta)}\left[1 + \cos\left(\frac{2\pi}{\Lambda}(\theta - \theta_{ar} \pm \frac{\chi}{2})\right)\right] & \theta_{ar} \mp \frac{\chi}{2} - \frac{\Lambda}{2} \leq \theta < \theta_{ar} \mp \frac{\chi}{2} + \frac{\Lambda}{2} \\ 0 & \theta \geq \theta_{ar} \mp \frac{\chi}{2} + \frac{\Lambda}{2} \end{cases} \quad (5)$$

In terms of these piecewise functions $G(\theta)$ becomes:

$$G(\theta) = \frac{1}{\sin\theta}\int_0^{\theta}[B_-(\theta') + B_+(\theta')]\sin(\theta')d\theta'. \quad (6)$$

A model AR is shown in Figure 2-b. This AR is located at a latitude of 40^o and has a penetration depth of $0.85R_{\odot}$. The depth of penetration of the AR is motivated from results indicating that the disconnection of an AR flux-tube happens deep down in the CZ[30].

4 Recreating the Poloidal Field

Given that the accumulated effect of all ARs is what regenerates the poloidal field, we need to specify an algorithm for AR eruption and decay in the context of the solar cycle. For each hemisphere independently and on each solar day of our simulation we perform the following procedure:

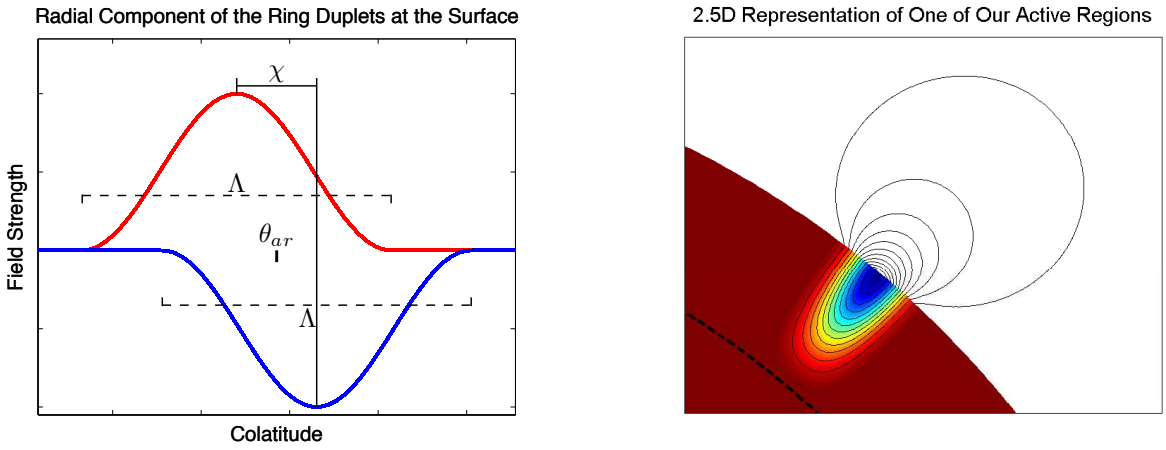

(a) (b)

Figure 2: (a) Superimposed magnetic field of the two polarities of a modeled active region (tilted bipolar sunspot pair). The different quantities involved are: the co-latitude of emergence θ_{ar}, the diameter of each polarity of the duplet Λ and the latitudinal distance between the centers χ. (b) Field lines of one of our model active regions including a potential field extrapolation for the region outside of the Sun. Contours correspond to field lines that trace the poloidal components and in this example their sense is counter-clockwise. The dashed line is included for reference and corresponds to a depth of $0.85R_{\odot}$.

1. Search for magnetic fields exceeding a critical buoyancy threshold $B_c = 5 \times 10^4$ Gauss on a specified layer at the bottom of the CZ ($r = 0.71R_{\odot}$), and record their latitudes.

2. Choose randomly one of the latitudes found on Step 1 and calculate the amount of magnetic flux present within it's associated toroidal ring. The probability distribution we use is not uniform, but is restricted to observed active latitudes. We do this by making the probability function drop steadily to zero between 30^o (-30^o) and 40^o (-40^o) in the northern (southern)

hemisphere:

$$P(\theta) \propto \left(1 + \mathrm{erf}\left[\frac{\theta - 0.305\pi}{0.055\pi}\right]\right)\left(1 - \mathrm{erf}\left[\frac{\theta - 0.694\pi}{0.055\pi}\right]\right). \quad (7)$$

3. Calculate the corresponding AR's tilt, using the local field strength B_0, the calculated flux Φ_0 and the latitude of emergence λ. For this we use the expression found by Fan, Fisher & McClymont[31] ($\gamma \propto \Phi_0^{1/4} B_0^{-5/4} \sin(\lambda)$).

4. Reduce the magnetic field of the toroidal ring from which the AR originates. In order to do this, we first estimate how much magnetic energy is present on a partial toroidal ring (after removing a chunk with the same angular size as the emerging AR). Given that this energy is smaller than the one calculated with a full ring, we set the value of the toroidal field such that the energy of a full toroidal ring filled with the new magnetic field strength is the same as the one calculated with the old magnitude for a partial ring.

5. Deposit an AR (as defined in Section 3), at the same latitude chosen on Step 2, whose strength is determined by the flux calculated in Step 2 and whose tilt was calculated on Step 3.

5 Meridional Flow

We use the meridional profile of Muñoz-Jaramillo, Nandy and Martens[24] (MNM09), which closely represents the observed features present in helioseismic meridional flow data and is defined by the following stream funcion:

$$\Psi(r,\theta) = \frac{v_0(t)}{r}(r - R_p)(r - R_\odot)\sin\left(\pi\frac{r - R_p}{R_1 - R_p}\right)^a \sin^{(q+1)}(\theta)\cos(\theta), \quad (8)$$

where $q = 1$ governs the latitudinal dependence, $R_p = 0.675R_\odot$ the penetration depth, $a = 1.92$ and $R_1 = 1.029R_\odot$ govern the location of the peak of the poleward flow and the amplitude and location of the equatorward return flow. For more details please refer to MNM09[24]. In order to test the impact of a changing meridional flow on the solar cycle, $v_0(t)$ is set such that the peak amplitude of the meridional flow at the surface varies between $15-30$m/s. We track the polar field amplitude and produce random changes in $v_0(t)$ at sunspot maximum.

6 Differential Rotation

We use the analytical form of Charbonneau et al.[32]. It is defined as:

$$\Omega_A(r,\theta) = 2\pi\left[\Omega_c + \tfrac{1}{2}\left(1+\mathtt{erf}\left(\tfrac{r-r_{tc}}{w_{tc}}\right)\right)(\Omega_e - \Omega_c + (\Omega_p-\Omega_e)\Omega_S(\theta))\right] \tag{9}$$

$$\Omega_S(\theta) = a\cos^2(\theta) + (1-a)\cos^4(\theta),$$

where $\Omega_c = 432$ nHz is the rotation frequency of the core, $\Omega_e = 470$ nHz is the rotation frequency of the equator, $\Omega_p = 330$ nHz is the rotation frequency of the pole, $a = 0.483$ is the strength of the $\cos^2(\theta)$ term relative to the $\cos^4(\theta)$ term, $r_{tc} = 0.7R_\odot$ the location of the tachocline and $w_{tc} = 0.025R_\odot$ half of its thickness.

7 Turbulent Magnetic Diffusivity

The final ingredient of this model is a radially dependent magnetic diffusivity; in this work we use a double-step profile given by

$$\eta(r) = \eta_{bcd} + \frac{\eta_{cz} - \eta_{bcd}}{2}\left(1 + \mathrm{erf}\left(\frac{r - r_{cz}}{d_{cz}}\right)\right) + \frac{\eta_{sg} - \eta_{cz} - \eta_{bcd}}{2}\left(1 + \mathrm{erf}\left(\frac{r - r_{sg}}{d_{sg}},\right)\right) \quad (10)$$

where $\eta_{bcd} = 10^8$ cm^2/s corresponds to the diffusivity at the bottom of the computational domain, $\eta_{cz} = 10^{11}$ cm^2/s corresponds to the diffusivity in the convection zone, $\eta_{sg} = 10^{12}$ cm^2/s corresponds to the near-surface supergranular diffusivity and $r_{cz} = 0.71R_\odot$, $d_{cz} = 0.015R_\odot$, $r_{sg} = 0.95R_\odot$ and $d_{sg} = 0.025R_\odot$ characterize the transitions from one value of diffusivity to the other.

8 Numerical Methods

In order to solve the 2.5 dynamo equations (Eq. 1 & 2) we transform our system of Partial Differential Equations(PDEs) to a system of coupled Ordinary Differential Equations(ODEs) by discretizing the spatial operators using finite differences. For advective terms we use a third order upwind scheme, for diffusive terms we use a second order space centered scheme and for other first derivative terms we use a second order space centered scheme. We then use an exponential propagation method to integrate the equations in time[24,33,34].

Our computational domain comprises the entire solar convection zone and a small section of the upper radiative region ($0.55R_\odot \leq r \leq R_\odot$ and $0 \leq \theta \leq \pi$). We use a 300×500 uniformly

spaced grid in radius (300 points) and colatitude (500 points). Our boundary conditions are:

$$\begin{aligned} &A(r,\theta=0)=0, \quad \tfrac{\partial(rA)}{\partial r}|_{r=R_\odot}=0, \quad A(r,\theta=\pi)=0, \quad A(r=0.55R_\odot,\theta)=0 \\ &B(r,\theta=0)=0, \quad B(r=R_\odot,\theta)=0, \quad B(r,\theta=\pi)=0, \quad \tfrac{\partial(rB)}{\partial r}|_{r=0.55R_\odot}=0, \end{aligned} \tag{11}$$

which correspond to a conductive core at $r = 0.55R_\odot$, a perfect vacuum at $r = R_\odot$ and the rotation axis in an axisymmetric formulation at $\theta = 0, \pi$.

9 Sensitivity to Changes in the Simulation Setup

The representative simulation results presented earlier (which we term as the reference solution) were performed with the parameters and model setup as described in previous sections. Our realistic method of handling solar active regions is a major improvement within the framework of solar dynamo models and has been demonstrated to capture accurately the observed surface flux transport dynamics leading to polar field reversal[7]. The internal meridional flow profile that we have used is based on the best available constraints from helioseismic data[20,24] and the standard model of the solar interior[35]. In our simulations we have used a peak speed randomly varying between a reasonable range while keeping the internal profile unchanged and as constrained in MNM09[24]. This variation is assumed to be instantaneous in our reference simulations. The internal diffusivity profile in our simulations is widely used in the community (see the dynamo benchmark study by Jouve et al.[36] and the review by Charbonneau[6]); however, the assumed value of the turbulent diffusivity coefficient can be different in various simulations. This value sets the diffusive timescale and determines whether flux transport dynamics is dominated by diffusion or advection by meridional flow[17]. In this section, we test the robustness of our results to changes in those aspects of our

model setup which are not well constrained.

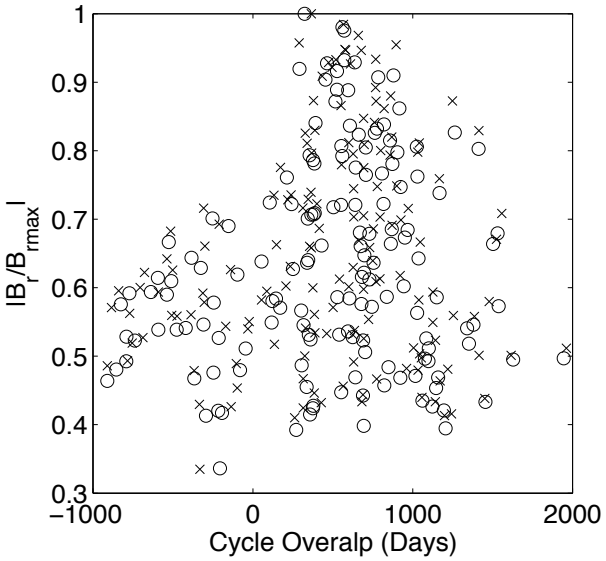

Figure 3: Simulated normalized polar field strength versus cycle overlap at sunspot cycle minimum in units of days for a run with supergranular diffusivity of 5×10^{12} cm^2/s. Here, $B_{max} = 9.62 \times 10^3$ Gauss.The results show that even in a high-diffusivity solution, a deep solar minimum with a large number of spotless days is typically associated with relatively weak polar field strength as indicated by the reference simulation. Crosses (circles) correspond to data from the Northern (Southern) solar hemisphere

We first study the impact of varying the meridional flow continuously between the old and the new random value (as opposed to the instantaneous change in our reference solutions). As outlined in Tables 1–2, the correlations between cycle overlap, polar field strength and meridional flow variations remain very similar (both qualitatively and quantitatively) to that obtained earlier in our reference solution. In fact, in certain cases the correlations become stronger on incorporating

smoothly varying meridional flows.

Furthermore, we explore the influence of a higher turbulent diffusion coefficient with a new model run, keeping other ingredients the same as in the reference solution. With a diffusivity coefficient five times that of the reference solution in the upper part of the convection zone (which increases the role of diffusive flux transport in this region) we find that the results remain qualitatively similar, although quantitatively somewhat different. The flow speed in the early half of the cycle (v_{n-1}) still has the maximum impact on the number of spotless days (conversely, cycle overlap), although the strength of the correlation is weaker relative to the reference solution. This is expected as in these model runs, diffusive flux dispersal shares the responsibility of magnetic flux transport along with meridional circulation thereby somewhat reducing the correlation between flow speed and cycle overlap. Additionally, we find that the correlation between the polar field strength and meridional flow speed in these high diffusivity solutions is essentially similar to that of the reference solution.

Note that the toroidal and poloidal field strength are determined by the threshold for magnetic buoyancy in these kinematic simulations. In the reference solution we have set $B_c = 5 \times 10^4$ Gauss based on results of thin-flux-tube-simulations. The peak polar (radial) field strength generated in this simulation is 16.66×10^3 Gauss (9.62×10^3 Gauss for the high-diffusivity solution with the same B_c). However, full-MHD simulations can self-consistently generate toroidal field strength only on the order of 1000 Gauss[37]. We have performed additional runs with a new buoyancy

kinematically simulated toroidal field amplitude on the same order as that in full-MHD simulations. As indicated in the accompanying tables, the relationship between the nature of solar minima and flow speed variations remain the same qualitatively as in the reference solution. We also find that in this case, the peak polar field strength reduces to 147 Gauss. Although low-resolution magnetograms which measure the (plausibly unresolved) diffuse component of the magnetic field indicate that the average field strength is on the order of tens of Gauss, recent high resolution observations from the Hinode space mission shows the existence of strong kilo-Gauss unipolar (radial) flux tubes in the polar region[38,39]. Although, it is not clear whether in reality the strong kilo-Gauss flux tubes or the much weaker (diffuse) polar field is involved in the regeneration of the toroidal field, our numerous model runs show that this is a matter of scaling; the underlying qualitative relationship between the characteristics of solar minima and flow variations remain similar.

Finally, we explore the correlation between cycle overlap and polar field strength (Table 3). We find that in the simulation using continuously varying meridional flows, the correlation is actually stronger in comparison to the reference solution. In the high diffusion case the correlation between cycle overlap and polar field strength is almost negligible; interestingly, however, a similar trend to the reference solution is still apparent (Figure 3); cycles with a large number of spotless days (high negative overlap) have consistently weaker polar field strength.

In summary therefore, we find that the main model results related to the origin of very deep solar minima is robust with respect to reasonable changes in the simulation setup and assumptions.

10 A Note on Flow Observations

How do our simulations compare to flow observations related to the minimum of solar cycle 23? Helioseismic measurements of the equatorward migration of the solar internal torsional oscillation show that the torsional oscillation pattern of the upcoming cycle 24 (which originated near the maximum of the preceding cycle) is migrating relatively slowly compared to that of cycle 23[40]. Since the torsional oscillation pattern is believed to be associated with the migration of the magnetic cycle[27], this could be indirect evidence that the meridional flow driving (the toroidal field belt of) cycle 24 in the solar interior is relatively slow compared to that of the previous cycle; this is in agreement with our theoretical simulations.

On the other hand, direct surface observations[41] indicate that the flow near the surface may have increased (roughly in a sinusoidal fashion) from the maximum of cycle 23 to its minimum – in apparent conflict with the earlier, indirect evidence of a slower flow and our simulations. However, helioseismic measurements indicate that these near-surface flow variations reduce with depth and is almost non-existent at depths of 0.979 $R_\odot$[42]. Therefore we argue that these surface variations may have no significant impact on the magnetic field dynamics in the solar interior, which is reflected in their inadequacy in reproducing the very low polar field strength at the minimum of cycle 23[28]. In support of our argument, we plot in Figure 4 the depth-dependence of the cumulative poleward mass flux amplitude in the meridional flow (based on a standard meridional flow profile) and find that only about 2% of the poleward mass-flux is contained within the surface and a depth of 0.975 $R_\odot$. Evidently, much of the flux transport dynamics associated with meridional flow occur deeper

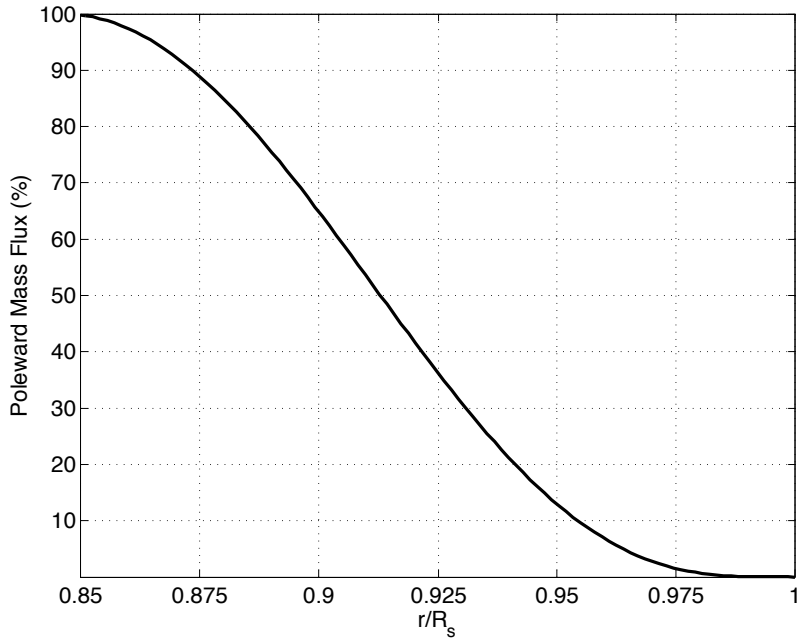

Figure 4: A plot of the cumulative meridional flow mass flux amplitude (between the radius in question and the surface; y-axis) versus depth (measured in terms of fractional solar radius $r/R_\odot$; x-axis). The mass flux is determined from the typical theoretical profile of meridional circulation used in solar dynamo simulations including the one described here. This estimate indicates that only about 2% of the poleward mass-flux is contained between the solar surface and a radius of 0.975 $R_\odot$, a region in which current (well-constrained) observations of the meridional flow is limited to.

down in the solar interior – as yet inaccessible to observations – probing which is possible using dynamo simulations such as that outlined here.

Simulation	Ovrlp. vs. V_n		Ovrlp. vs. V_{n-1}		Ovrlp. vs. ΔV_{n-1}	
	r	p	r	p	r	p
Northern Hemisphere						
1. Reference Solution	-0.13	93.42%	-0.81	99.99%	0.45	99.99%
2. Continuous Flow Variations	-0.13	94.28%	-0.80	99.99%	0.47	99.99%
3. High Diffusivity	-0.17	97.00%	-0.38	99.99%	0.15	93.46%
4. Low Buoyant Threshold (1KG)	-0.20	99.75%	-0.63	99.99%	0.30	99.99%
Southern Hemisphere						
1. Reference Solution	-0.13	94.53%	-0.80	99.99%	0.45	99.99%
2. Continuous Flow Variations	-0.13	94.32%	-0.79	99.99%	0.46	99.99%
3. High Diffusivity	-0.17	96.61%	-0.38	99.99%	0.15	93.66%
4. Low Buoyant Threshold (1KG)	-0.19	99.65%	-0.64	99.99%	0.31	99.99%

Table 1: Correlations for overlap versus meridional flow. (1) The reference solution uses all the parameters mentioned above and is the one reported in the main manuscript. (2) In this simulation the flow no longer changes abruptly but undergoes a continuous change from one value to the other through a ramp function. The slope is set such that the largest change (15 m/s) takes three years. (3) Solution in which the supergranular diffusivity is changed from $\eta_{sg} = 10^{12}$ cm^2/s to $\eta_{sg} = 5 \times 10^{12}$ cm^2/s. (4) Simulation in which the buoyant threshold is 1 kilo-Gauss (KG).

Simulation	Br vs. V_n		Br vs. V_{n-1}		Br vs. ΔV_{n-1}	
	r	p	r	p	r	p
Northern Hemisphere						
1. Reference Solution	0.45	99.99%	-0.83	99.99%	0.87	99.99%
2. Continuous Flow Variations	0.40	99.99%	-0.82	99.99%	0.91	99.99%
3. High Diffusivity Solution	0.39	99.99%	-0.68	99.99%	0.76	99.99%
4. Low Buoyant Threshold (1KG)	0.43	99.99%	-0.74	99.99%	0.78	99.99%
Southern Hemisphere						
1. Reference Solution	0.45	99.99%	-0.83	99.99%	0.87	99.99%
2. Continuous Flow Variations	0.40	99.99%	-0.81	99.99%	0.91	99.99%
3. High Diffusivity Solution	0.38	99.99%	-0.68	99.99%	0.75	99.99%
4. Low Buoyant Threshold (1KG)	0.43	99.99%	-0.74	99.99%	0.78	99.99%

Table 2: Correlations for polar field strength versus meridional flow. (1) The reference solution uses all the parameters mentioned above and is the one reported in the main manuscript. (2) In this simulation the flow no longer changes abruptly but undergoes a continuous change from one value to the other through a ramp function. The slope is set such that the largest change (15 m/s) takes three years. (3) Solution in which the supergranular diffusivity is changed from $\eta_{sg} = 10^{12}$ cm^2/s to $\eta_{sg} = 5 \times 10^{12}$ cm^2/s. (4) Simulation in which the buoyant threshold is 1 kilo-Gauss (KG).

Simulation	Br vs. Ovrlp.	
	r	p
Northern Hemisphere		
1. Reference Solution	0.46	99.99%
2. Continuous Flow Variations	0.54	99.99%
3. High Diffusivity	0.10	80.02%
4. Low Buoyant Threshold (1KG)	0.32	99.99%
Southern Hemisphere		
1. Reference Solution	0.47	99.99%
2. Continuous Flow Variations	0.52	99.99%
3. High Diffusivity	0.12	85.44%
4. Low Buoyant Threshold (1KG)	0.33	99.99%

Table 3: Correlations for polar field strength versus overlap. (1) The reference solution uses all the parameters mentioned above and is the one reported in the main manuscript. (2) In this simulation the flow no longer changes abruptly but undergoes a continuous change from one value to the other through a ramp function. The slope is set such that the largest change (15 m/s) takes three years. (3) Solution in which the supergranular diffusivity is changed from $\eta_{sg} = 10^{12}$ cm^2/s to $\eta_{sg} = 5 \times 10^{12}$ cm^2/s. (4) Simulation in which the buoyant threshold is 1 kilo-Gauss (KG).

References

29. Dasi-Espuig, M., Solanki, S. K., Krivova, N. A., Cameron, R. H. & Peñuela, T. Sunspot group tilt angles and the strength of the solar cycle. *Astron. Astrophys.* **518**, A7 (2010).

30. Longcope, D. & Choudhuri, A. R. The Orientational Relaxation of Bipolar Active Regions. *Sol. Phys.* **205**, 63–92 (2002).

31. Fan, Y., Fisher, G. H. & McClymont, A. N. Dynamics of emerging active region flux loops. *Astrophys. J.* **436**, 907–928 (1994).

32. Charbonneau, P. *et al.* Helioseismic Constraints on the Structure of the Solar Tachocline. *Astrophys. J.* **527**, 445–460 (1999).

33. Hochbruck, M. & Lubich, C. On Krylov subspace approximations to the matrix exponential operator. *SIAM Journal on Numerical Analysis* **34**, 1911–1925 (1997).

34. Hochbruck, M., Lubich, C. & Selhofer, H. Exponential integrators for large systems of differential equations. *SIAM Journal on Scientific Computing* **19**, 1552–1574 (1998).

35. Christensen-Dalsgaard, J. *et al.* The Current State of Solar Modeling. *Science* **272**, 1286–+ (1996).

36. Jouve, L. *et al.* A solar mean field dynamo benchmark. *Astron. Astrophys.* **483**, 949–960 (2008).

37. Ghizaru, M., Charbonneau, P. & Smolarkiewicz, P. K. Magnetic Cycles in Global Large-eddy Simulations of Solar Convection. *Astrophys. J.* **715**, L133–L137 (2010).

38. Tsuneta, S. *et al.* The Magnetic Landscape of the Sun's Polar Region. *Astrophys. J.* **688**, 1374–1381 (2008). 0807.4631.

39. Ito, H., Tsuneta, S., Shiota, D., Tokumaru, M. & Fujiki, K. Is the Polar Region Different from the Quiet Region of the Sun? *Astrophys. J.* **719**, 131–142 (2010). 1005.3667.

40. Howe, R. *et al.* A Note on the Torsional Oscillation at Solar Minimum. *Astrophys. J.* **701**, L87–L90 (2009). 0907.2965.

41. Hathaway, D. H. & Rightmire, L. Variations in the Sun's Meridional Flow over a Solar Cycle. *Science* **327**, 1350– (2010).

42. González Hernández, I., Howe, R., Komm, R. & Hill, F. Meridional Circulation During the Extended Solar Minimum: Another Component of the Torsional Oscillation? *Astrophys. J.* **713**, L16–L20 (2010). 1003.1685.